

Denoising Graph Super-Resolution towards Improved Collider Event Reconstruction

Nilotpal Kakati¹, Etienne Dreyer¹, Eilam Gross¹

¹ Weizmann Institute of Science

E-mail: nilotpal.kakati@weizmann.ac.il

September 2024

Abstract. Accurately reconstructing particles from detector data is a critical challenge in experimental particle physics, where the spatial resolution of calorimeters has a crucial impact. This study explores the integration of super-resolution techniques into an LHC-like reconstruction pipeline to effectively enhance the granularity of calorimeter data and suppress noise. We find that this software preprocessing step can significantly improve reconstruction quality without physical changes to detectors. To demonstrate the impact of our approach, we propose a novel particle flow model that offers enhanced particle reconstruction quality and interpretability. These advancements underline the potential of super-resolution to impact both current and future particle physics experiments.

Keywords: super-resolution, denoising, flow matching, reconstruction, diffusion transformers, graphs, attention, conditional generation

1. Introduction

In high-energy physics, accurate reconstruction of final state particles is essential for extracting information from collider experiments. This process hinges on localized measurements of energy deposits in detectors, where calorimeters play a key role. Calorimeters measure energy by instigating a shower of secondary particles, distributing and absorbing the incident particle's energy as it propagates through successive layers of dense material. To help determine particle direction and type, as well as separate nearby particles, calorimeters are segmented into a grid-like array of cells.

The main performance metric for calorimeters is energy resolution, determined by a number of material, electronic, and geometric factors. In practice, however, a calorimeter's spatial resolution (inversely related to its granularity) also significantly influences its particle reconstruction capabilities. This is especially true for general-purpose detectors at the Large Hadron Collider (LHC) [1] where abundant hadronic jets and simultaneous collisions create a highly dense environment. In this setting, calorimeter granularity drives the ability of reconstruction algorithms to correctly assign energy deposits to particle trajectories. This

assignment task is necessary to avoid double counting in particle flow (PFlow) algorithms [2, 3] where jet kinematics are determined based on the combined measurements of charged particle tracks and calorimeter clusters. Similarly, in software compensation [4], jet energy resolution can be improved by distinguishing electromagnetic sub-showers embedded in hadronic showers, a technique requiring excellent spatial resolution.

However, in practical applications, calorimeter design is constrained by cost, physical volume, and electronic readout, leading to less than optimal granularity. Super-resolution (SR) techniques, which have been extensively studied in the field of image processing [5–11], offer the potential to go beyond the spatial resolution intrinsic to the calorimeter design. By reconstructing high-resolution (HR) data from low-resolution (LR) inputs, these techniques could, in essence, enhance the granularity of calorimeter data without requiring physical modifications to the detector itself. Calorimeter SR was first explored in [12], which demonstrated a proof-of-concept using a neural network-based method with a simplified detector and physics setup. Since then, SR has found various applications in particle physics, such as enhancing jet constituent images with generative adversarial networks for improved jet property estimation [13], employing normalizing flows for upsampling calorimeter showers for fast simulation [14], and producing high-resolution photon shower images [15]. Recent work [16] also highlights its potential in enhancing event reconstruction for neutrino telescopes.

In this study, we explore the integration of super-resolution techniques within the core pipeline of particle reconstruction in collider experiments. The initial stage of any collider experiment involves reconstructing low-level particles or particle-like objects, referred to as PFlow objects. By applying super-resolution to calorimeter data, we aim to enhance the accuracy of PFlow objects and, thereby, that of higher-level objects used in physics analyses, such as jets, leptons, and photons. We anticipate our approach to be particularly applicable to physics scenarios such as boosted boson jets, top jets, and hadronic tau decays.

Specifically, our approach offers two enhancements to calorimeter data to benefit the downstream reconstruction task. The first is the suppression of electronic noise that distort recorded energy deposits, which we perform by training our model to denoise the energy in each cell. Second, our approach improves spatial resolution by predicting a high-granularity graph of calorimeter cells, allowing the reconstruction of finer details such as nearby particles. Representing the calorimeter data as a graph is a natural choice for handling irregular geometry, non-trivial spatial correlations, and the sparsity in the recorded signal. Super-resolution on graph data, where the number of nodes gets upscaled, is not an entirely new concept [17, 18] but is uncommon in the literature.

To assess the improvement in reconstruction, we introduce a novel transformer-based PFlow model, based on predicting hypergraphs, as introduced in [19]. This model benefits from modernized architecture and provides improved interpretability, allowing the impact of super-resolution to be analyzed transparently.

2. Datasets

To train the super-resolution model, we require the same calorimeter shower data in both low and high granularity (i.e. resolution). This was achieved using the COCOA package [20], which provides an LHC-like generic calorimeter model simulated with GEANT4 [21–23]. COCOA includes three electromagnetic (ECAL) and three hadronic (HCAL) concentric layers, each with configurable material, granularity and noise levels. The package emulates sampling fractions of $f = 0.07$ and $f = 0.025$ in the ECAL and HCAL, respectively, by using an effective molecule that represents the mixture of active (liquid Ar and plastic scintillator) and passive (Pb and Fe) materials. This is done by randomly dropping a fraction f of the shower segments and then scaling up the response in each cell by $1/f$. To focus solely on the calorimeter response, all upstream material, such as the inner tracker and solenoid iron, was removed, and the magnetic field was turned off, allowing showers from charged particles to propagate radially.

Table 1: Noise levels and granularity of the six calorimeter layers in both low and high resolution. The noise is only included for the low-granularity cells.

Layer		ECAL1	ECAL2	ECAL3	HCAL1	HCAL2	HCAL3
σ_{noise} [MeV]	(low)	13	34	41	75	50	25
η, ϕ segmentation single electron	(low)	128	128	64	32	16	8
	(high)	256	256	128	64	32	16
η, ϕ segmentation multi-particle	(low)	64	64	32	16	8	4
	(high)	256	256	128	64	32	16

In this study, we apply super-resolution exclusively in the pseudorapidity (η)-azimuthal angle (ϕ) plane, keeping the calorimeter layers unchanged. We use two datasets: the first is a simplified set where a single electron is fired with $p_T \in [50, 51]$ GeV, $\eta \in [-0.01, 0.01]$, and $\phi \in [-\pi, \pi]$. The second dataset involves multiple particles with angular separation on the scale of the calorimeter cells. The particles are arranged around a principle axis chosen uniformly in $\eta \in [-2.5, 2.5]$ and $\phi \in [-\pi, \pi]$. In three out of four cases, an electron is fired along the principle axis with $p_T \in [20, 50]$ GeV. The electron is accompanied by N photons with $p_T \in [5, 25]$ GeV where N is chosen randomly from 0 to 3 (and we ensure that at least one particle is fired). Each photon is displaced from the principle axis by $\pm \text{Gaus}(4 \cdot \delta, \delta)$ where the sign is chosen randomly and δ is the angular width of a cell in the high-resolution ECAL1. For the single electron dataset, the cell resolution is downsampled by factors, $f_\eta = f_\phi = 2$, and for the multi-particle dataset, by $f_\eta = f_\phi = 4$. Table 1 details the noise levels and granularity used for each calorimeter layer in this study.

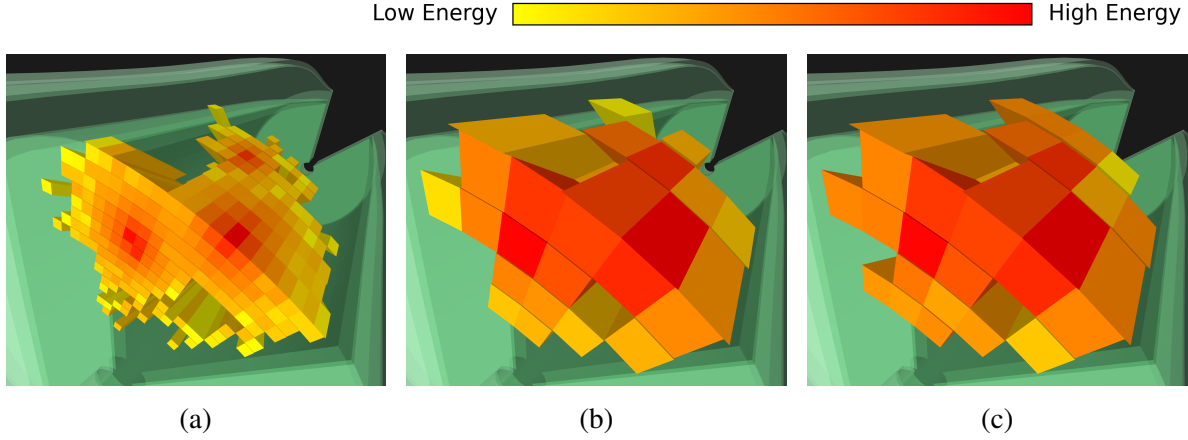


Figure 1: Phoenix event display [24] of one electron and two photons in COCOA, demonstrating the dataset creation procedure. Here we see (a) the truth high-resolution configuration, (b) the truth low-resolution configuration (c) the measured low-resolution configuration which also contains noise.

The particles interact with the high-resolution detector, initially with zero noise. The high-resolution cells are then combined to form low-resolution cells, to which noise is applied to simulate electronic noise. This procedure is illustrated in figure 1. Subsequently, the built-in topological clustering algorithm in COCOA, which resembles that of ATLAS, is used to cluster calorimeter hits based on energy-over-noise ratio thresholds. Only clustered cells with positive energy values are retained. Since our focus is on electromagnetic showers from electrons and photons, we limit our study to the ECAL layers.

3. Methods

3.1. Continuous normalizing flows

Continuous Normalizing Flow (CNF) [25] is a type of generative model that transforms a simple base probability distribution $p_0(x_0)$ into a more complex target distribution $p_1(x_1)$ through a continuous sequence of invertible transformations. This transformation is governed by the following neural ordinary differential equation (ODE):

$$\frac{dx}{dt} = v_\theta(x, t), \quad (1)$$

where v_θ is the vector field parameterised by a neural network and $t \in [0, 1]$. Flow Matching, as proposed in [26], is a technique for training continuous normalizing flows that aims to match the learned flow $v_\theta(t, x)$ induced by the differential equations of the model with a target flow $u_t(x)$. The flow-matching objective can be defined as follows:

$$L_{FM}(\theta) = E_{t, p_t(x)} \|v_\theta(t, x) - u_t(x)\|^2 \quad (2)$$

The objective, however, is intractable because the target flow, u_t , that generates the desired probability paths between p_0 and p_1 , is typically not available in closed form. As a solution,

[26] also proposed a conditional flow matching objective where u_t and p_t can be constructed in a sample-conditional manner:

$$L_{CFM}(\theta) = E_{t,q(z),p_t(x|z)} \|v_\theta(t, x) - u_t(x|z)\|^2, \quad (3)$$

where $t \in [0, 1]$, $z \sim q(z)$, $x \sim p_t(x|z)$. L_{CFM} is fully tractable and the authors showed that optimizing it is equivalent to optimizing the L_{FM} objective. The probability path, p_T , and the target flow, u_t , can be defined in various ways [26, 27]. For our studies, we use the formulation from the original paper [26]:

$$\begin{aligned} p_t(x|z) &= \mathcal{N}\left(x | tx_1, (t\sigma - t + 1)^2\right) \\ u_t(x|z) &= \frac{x_1 - (1 - \sigma)x}{1 - (1 - \sigma)t} \end{aligned} \quad (4)$$

This defines a straight path between the standard normal and a Gaussian distribution of width σ around x_1 . We chose σ to be 10^{-4} following the original paper. We used the `torchdiffeq` [28] library with the Dormand-Prince (`dopri5`) solver for generation.

3.2. Super Resolution model

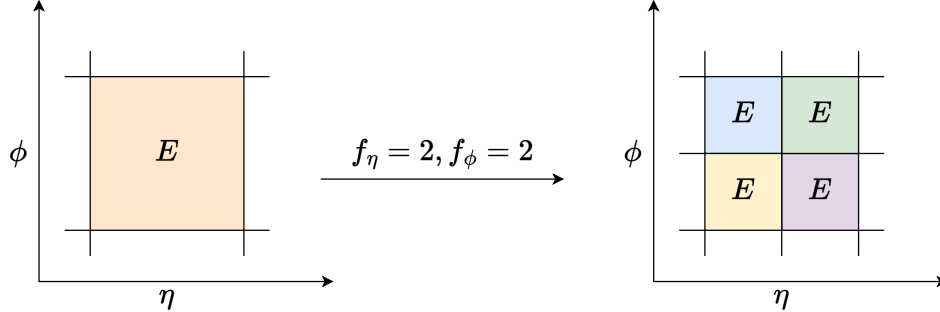


Figure 2: Creation of high-resolution cell in our approach. Each low-resolution cell is split in η and ϕ by the super-resolution factor f_η and f_ϕ , respectively. They get their new angular coordinates and the parent low-resolution energy (E) is copied to serve as the conditional inputs. Here, we see the procedure for $f_\eta = 2$ and $f_\phi = 2$. Each cell is a node in the graph, but for illustrative purpose, we are denoting them as images.

The core concept of our super-resolution model is inspired by the work [11]. To allow for irregular cell geometry and to cope with the sparsity of the recorded energy deposits, we represent the data as graphs. Each low-resolution graph is expanded into a high-resolution graph, where each low-resolution cell is divided into $f_\eta \times f_\phi$ high-resolution cells. For each high-resolution cell, the target is its truth energy value, while the corresponding low-resolution energy serves as the conditional input, as illustrated in figure 2. Although nearest-neighbor edges among nodes in the high-resolution graph would, in general, be motivated for larger graphs, we model them as fully connected for simplicity.

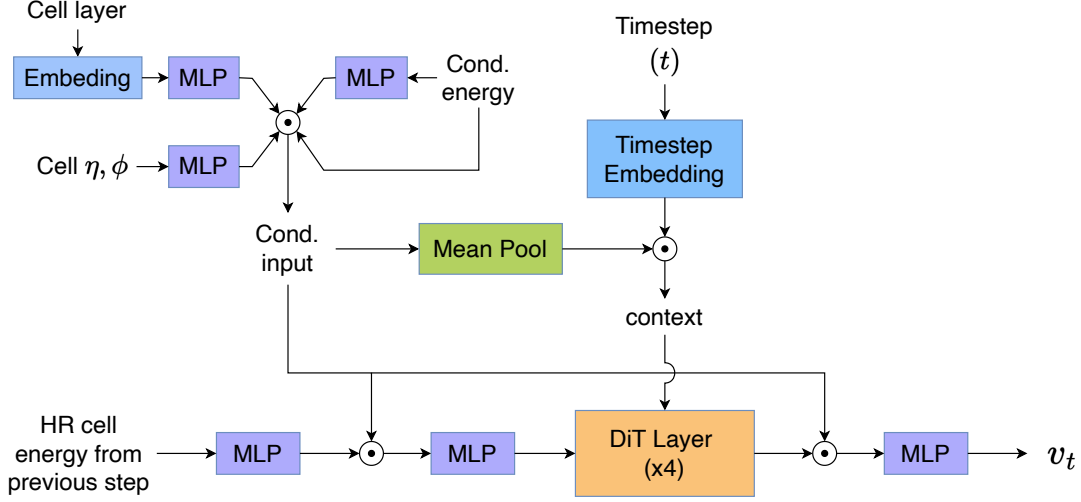


Figure 3: The super-resolution architecture. \odot indicates concatenation.

Our model adopts a transformer-based architecture to predict the vector field, v_θ , as shown in figure 3. For each high-resolution cell, the conditional input includes its geometric location and the energy of its corresponding low-resolution cell. Since the cell layer is a discrete quantity, we first embed it into a three-dimensional vector space. The angular positions (η , ϕ), the embedded layer, and the low-resolution parent energy are each processed through separate multi-layer perceptrons (MLPs). The outputs of these MLPs are concatenated, along with a skip connection from the low-resolution parent cell energy, to form the conditional inputs for each high-resolution cell.

The transformer’s input consists of the conditional input and the high-resolution cell energy from the previous step. This energy is first processed through an MLP, concatenated with the conditional input, and then passed through another MLP before being fed into the transformer. We employ a specific transformer architecture known as the *diffusion transformer* (DiT) as proposed in [29]. The average of the conditional input across all cells, combined with the embedded timestep, serves as the context required for the adaptive layer normalization (adaLN) operations in DiT. This transformer architecture enables the generation of enriched cell representations that are contextually aware of their surroundings, enhancing the model’s ability to learn the shower profiles.

Instead of directly using the high-resolution cell energy as the target, we employ a method inspired by the approach outlined in [30]. For each high-resolution cell, we compute the ratio between the target high-resolution energy and the corresponding measured low-resolution energy, scaled by a scaling factor f (equation 5). This ratio is then clamped to be in $[0, 1]$. Subsequently, a transformation is applied to this clamped ratio, converting it to a new scale (equation 6). Finally, the logit of this transformed value is used as the training target (equation 7). This procedure effectively allows the network to learn corrections to the raw energy estimates, facilitating easier learning and increasing robustness to out-of-distribution data.

$$\text{ratio}, r_i = \text{clamp} \left(\frac{E_i^{HR}}{f \cdot E_i^{LR}} \right) \quad (5)$$

$$r'_i = \alpha + (1 - 2\alpha) r_i \quad (6)$$

$$\text{target}_i = \ln \left(\frac{r'_i}{1 - r'_i} \right) \quad (7)$$

The hyperparameters used during training are summarized in table 2. For the single electron study, the training, validation, and test datasets consisted of 1,000,000, 3,000, and 10,000 events, respectively. In the multi-particle study, we utilized 250,000 events for training, 3,000 for validation, and 10,000 for testing.

Hyperparameter	
Batch size	25
Optimizer	AdamW [31]
Learning rate	0.001
Number of epochs	100
Number of time steps	25
Number of DiT layers	4
Number of trainable parameters	4.2M

Table 2: Hyperparameters used in the super-resolution model.

3.3. Ensemble sampling

Generation with CNF is inherently a stochastic process. While this randomness is often beneficial in applications like image generation, where variation is desired, it poses a challenge in the super-resolution of calorimeter data, where there is a specific deterministic target. Ideally, the network’s output should fluctuate around the true target if functioning correctly. To address this, we employ an ensemble approach. Unlike typical ensemble methods that involve training multiple copies of the model, our approach simply involves passing the same conditional input through the same model multiple times to produce the ensemble output, which is then averaged to obtain the final prediction. This technique helps reduce the impact of fluctuations and brings the output closer to the true target. However, it is important to acknowledge that due to the stochastic noise inherently added by the calorimeter, recovering the exact true energy is not possible; we can only approximate it.

3.4. Particle-flow model

Machine learning-based particle flow models for LHC-like environments have been extensively explored [19, 32–39]. Among these, *HGPflow* [19] offers the most transparent and interpretable architecture. To better understand the impact of super-resolution, we aimed for a similarly transparent model. Here, we present a novel particle flow (Pflow) model that builds on the principles of *HGPflow* but replaces the *iterative learning* approach with a *supervised attention* mechanism. The architecture, depicted in figure 4, consists of three main components: the encoder, the cardinality predictor, and the kinematic predictor.

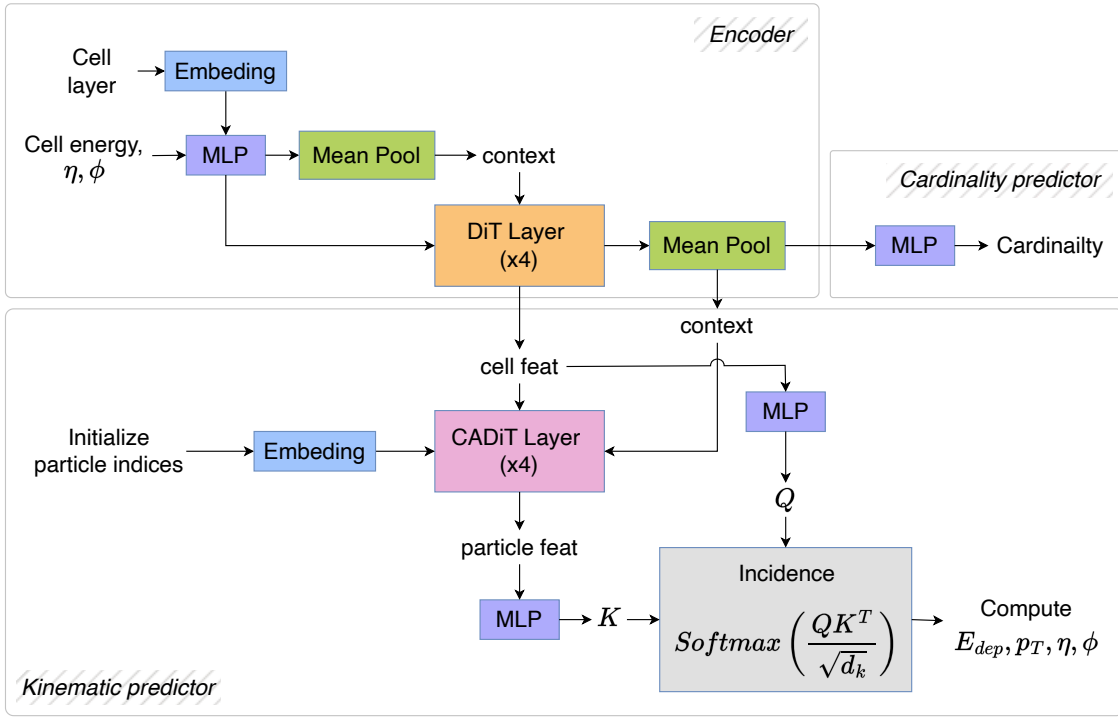


Figure 4: The Particle flow architecture. \odot indicates concatenation.

Encoder: The encoder begins by mapping the cell features—cell energy, angular position (η, ϕ), and embedded cell layer—into a high-dimensional vector space. These features are processed through four DiT layers to construct a neighborhood-aware representation. The average representation across all cells is used as a context input for the DiT layers. This mean-pooled output of the DiT block is then passed to both the cardinality predictor and the kinematic predictor.

Cardinality Predictor: The cardinality predictor is a simple MLP that takes the encoder’s output as input. We approach cardinality prediction as a classification task rather than regression. While predicting cardinality as a global metric is not the most robust approach, and many existing models [19, 36] handle this as a padding problem, predicting a flag for each particle to indicate if it’s real or padded, we opted for a simpler classification approach

given our lower cardinality and simpler environment. In principle, switching to the padding approach is straightforward and will be considered in future work.

Kinematic Predictor: The kinematic predictor requires the number of particles in an event as input. During training, we use the true cardinality; during inference, we rely on the cardinality predictor’s output. We initialize particle indices, embed them into a four-dimensional vector space, and process them through an MLP. The encoded particles and cells are passed through four CADiT layers. Within each layer, cross-attention is first performed between particles and cells, followed by particle updates using self-attention. The mean-pooled representation from the encoder’s cells serves as the context for these CADiT layers.

The kinematic predictor aims to learn the fractional energy distribution of each cell over the particles, as shown in equation 8, where E_{ai} represents the energy deposited by particle a in cell i . This distribution, referred to as the incidence matrix in HGPflow [19], was originally defined for topological clusters rather than individual cells. By using cells directly, we retain more detailed information, as topological clusters aggregate the features of multiple cells, potentially losing fine-grained details. While working with cells increases the complexity due to higher cardinality—potentially by an order of magnitude or more compared to clusters—it eliminates the dependency on topoclustering, which is not guaranteed to be an optimal algorithm. We implement this approach using an attention-like framework, where particles and cells are processed through two MLPs to obtain the key (K) and query (Q), respectively. The resulting attention weights are computed as usual (equation 9) and supervised to match the target incidence matrix. Given that we operate on sets, permutation invariance of particles is essential, and we achieve this using Hungarian matching [40].

$$\text{Target incidence, } I_{ai} = \frac{\text{energy deposited by particle } a \text{ in cell } i}{\text{total energy deposited in cell } i} = \frac{E_{ai}}{\sum_a E_{ai}} \quad (8)$$

$$\text{Predicted incidence} = \text{Attention weights} = \text{Softmax} \left(\frac{QK^T}{\sqrt{d_K}} \right) \quad (9)$$

Once the energy-based incidence matrix is determined, the *proxy* kinematics of the reconstructed particles can be calculated from the associated cells using the approach outlined in [19]

$$\begin{aligned} \hat{E}_a &= \sum_i (I_{ai} \cdot E_i); & \hat{\eta}_a &= \frac{1}{\hat{E}_a} \sum_i (I_{ai} \cdot E_i \cdot \eta_i); & \hat{\phi}_a &= \frac{1}{\hat{E}_a} \sum_i (I_{ai} \cdot E_i \cdot \phi_i) \\ \hat{p}_{Ta} &= \frac{\hat{E}_a}{\cosh \hat{\eta}_a} \quad (\text{zero mass assumption}) \end{aligned} \quad (10)$$

In HGPflow [19], these proxy properties are further refined using MLPs, a step we have omitted for this study. Given that our focus is on understanding the relative improvement from super-resolution in a simplified environment, we avoid relying on "blackbox" MLPs for major corrections. However, from a purely reconstruction perspective, adding a *correction network* would likely improve performance.

We trained two identical models using the same set of hyperparameters: one with the low-resolution measured cells and the other with the high-resolution predicted cells. The particle flow study utilized the same set of events from the multi-particle super-resolution study described earlier. For the incidence loss, we followed a procedure similar to that in [19], pairing truth and predicted particles using the Hungarian algorithm with the Kullback–Leibler divergence (KLD) between their incidence values as the metric. Cardinality loss was handled using cross-entropy, and the sum of the incidence and cardinality losses was used for optimization. The hyperparameters used for training are summarized in table 3.

Hyperparameter	
Batch size	30
Optimizer	AdamW [31]
Learning rate	0.001
Number of epochs	100
Number of encoder DiT layers	3
Number of CADiT layers	4
Number of trainable parameters	333K

Table 3: Hyperparameters used in the particle flow model.

4. Results

4.1. Single electron

Figure 5 provides a qualitative view of super-resolution applied to a single electron event. The predicted high-resolution cell energies closely align with the true values, and the time evolution of these predicted energies is also shown. Given that the target definition involves a correction to the input energy, the $t = 0$ state is not entirely random but instead closely reflects the conditional input. The network also manages to suppress noise as seen from the figure.

To quantitatively assess the impact on reconstruction, we estimate the electron’s energy by summing the energies of all cells in the event. We examine the energy residuals using both the measured low-resolution cell energies and the predicted high-resolution cell energies, with the target being the sum of the true high-resolution cell energies. Figure 6a illustrates these residual distributions. As discussed in section 3.3, the predicted high-resolution energies result from ensemble sampling, with an ensemble size of 10 in this instance. The figure shows that the high-resolution residual is much closer to zero and exhibits a narrower spread. The peak shift in the low-resolution distribution is due to the asymmetric noise contribution, as we retain only the cells with positive energy. The network effectively adapts to this asymmetric noise, demonstrating an improvement in energy resolution.

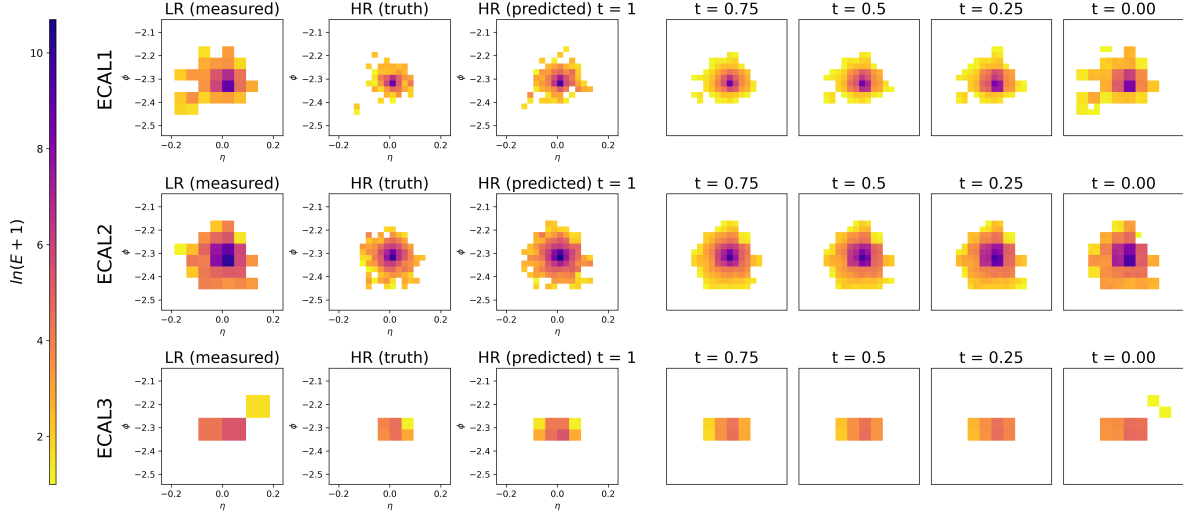


Figure 5: Super-resolution applied to a single electron event from the test set. The three rows depict the super-resolution process for the three ECAL layers. For each layer, the measured LR cell energy distribution, the target HR cell energy distribution, and the predicted HR are shown. The predicted HR cells closely matches the truth HR ones. Additionally, the time evolution of the cell energy distribution is also illustrated.

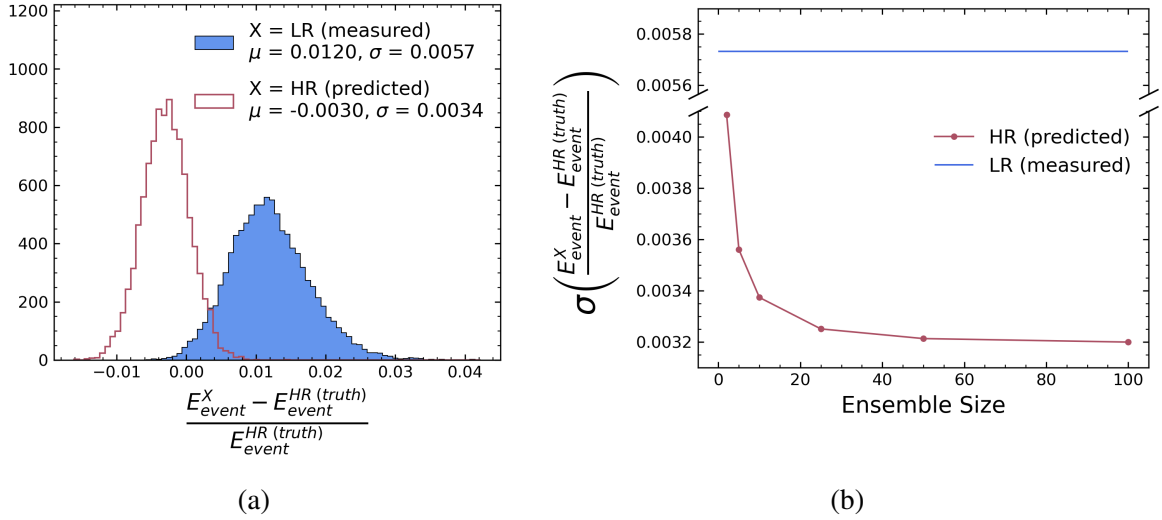


Figure 6: (a) The event level relative energy residual for the LR measured cell energy and the HR predicted cell energies with an ensemble size of 10 (b) The one- σ width of the event level residual distributions for the predicted cell energies as a function of the ensemble size.

We also examine how the performance depends on the ensemble size. As expected, the position of the residual distribution remains unchanged regardless of the ensemble size, and the width of the distribution varies. Figure 6b illustrates how the 1σ width of the residual distribution decreases as the ensemble size increases, with the improvement saturating above an ensemble size of 20. For all our studies, both for the single electron sample and the multi-

particle sample, we opted for an ensemble size of 10, to keep the computational costs lower while still benefiting from the advantages of ensemble sampling.

In addition, we analyzed the energy correlator observables C_2 , C_3 , and D_2 [41, 42] at the cell level for both high-resolution and low-resolution data. Figure 7 presents the resulting distributions, with lower values indicating more substructure. The predicted high-resolution cells closely match the true distribution and offer significant improvements over the noisy low-resolution data across all three substructure observables considered.

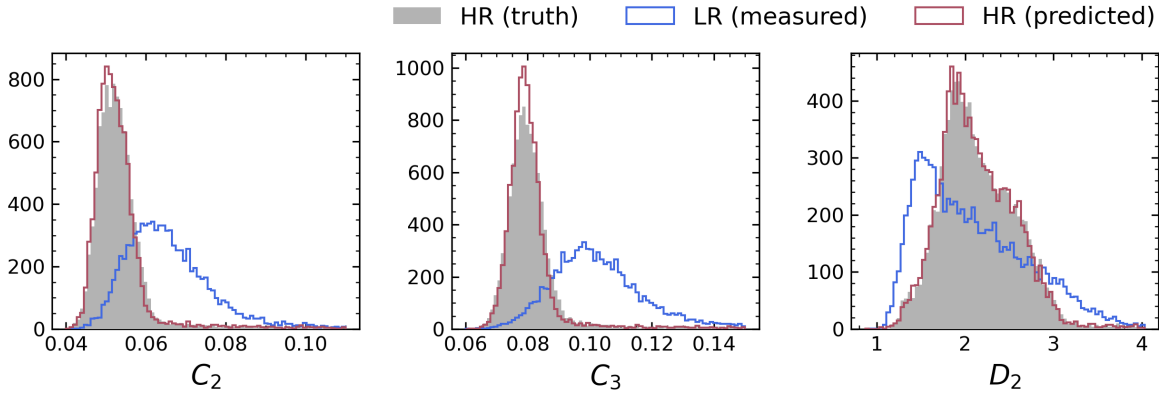


Figure 7: Substructure distributions for the truth high-resolution, measured low-resolution and predicted high-resolution cell energies.

4.2. Multiple particles

For the multi-particle sample, the most exciting aspect of the study is the impact on PFlow performance. We begin by examining the cardinality performance of the two networks, as summarized in table 4. Across the board, the network trained with predicted high-resolution cells shows either comparable or improved performance relative to the one trained with low-resolution measured cells. Both networks almost perfectly identify single-particle events, but as the true cardinality increases, their performance degrades—though at a slower rate for the network trained with high-resolution cells. When the true cardinality reaches its maximum, both networks exhibit similar performance, as this represents an edge-case scenario.

Next, we evaluate the performance of the computed particle p_T , η , and ϕ values derived from the incidence predictions. Ideally, the kinematic model would receive the predicted cardinality as input during inference. However, to isolate the performance of the kinematics predictor from the cardinality predictor, we instead use the true cardinality as input. To evaluate the kinematics at the particle level, we pair the true and predicted particles per event through Hungarian matching, using the KLD loss between their incidence values as the cost matrix. The p_T , η , and ϕ residuals after matching are shown in figure 8. Both models perform well in modeling the kinematic values, but the model trained on predicted high-resolution cells shows a marked improvement.

Truth cardinality	Accuracy	
	LR (measured)	HR (predicted)
1	99.38 %	99.41 %
2	88.52 %	91.02 %
3	77.62 %	81.97 %
4	81.32 %	81.42 %

Table 4: Cardinality prediction with the network trained on the LR cells with measured energy, compared with the network trained on the HR cells with predicted energy.

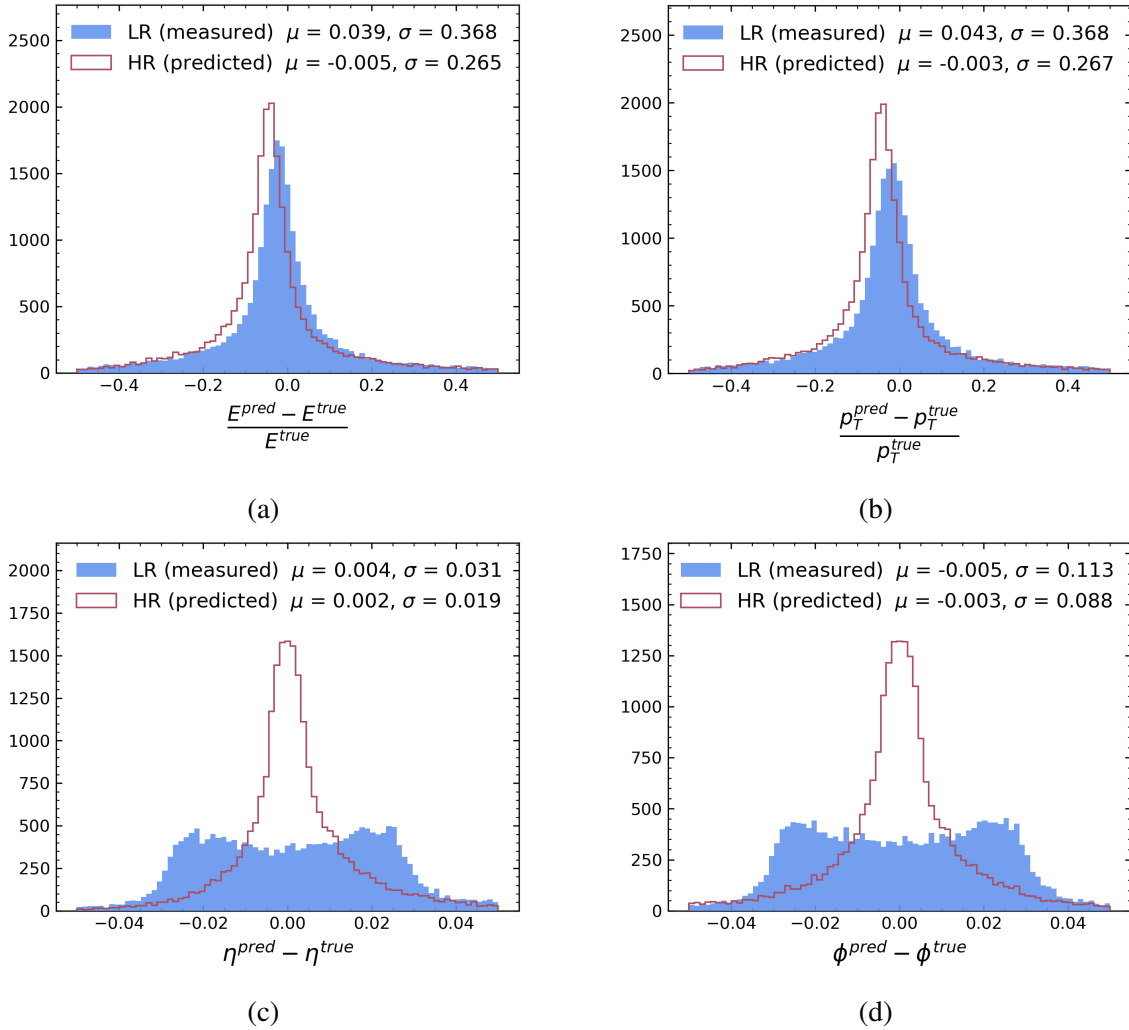


Figure 8: Particle flow performance (a) The relative energy residuals, (b) The relative transverse momentum residuals, (c) The pseudo-rapidity residuals, and (d) The azimuthal angle residuals between the truth particles and the reconstructed particles with Pflow model trained on measured low-resolution cells and the predicted high-resolution cells.

When a particle interacts with calorimeter cells, it often deposits a significant portion of its energy in a single cell, making that cell "hotter" than the others. Consequently, the η and ϕ values computed from the incidence matrix tend to gravitate towards those of the hottest cells. This results in the predicted particles not spreading evenly across the continuous space but instead forming diffused clumps at the midpoints of the highest resolution cells—in our case, the cells in the ECAL1 layer. This clustering effect is the reason we observe the slightly bimodal structure in figures 8c and 8d for the low-resolution model. Although the high-resolution model should theoretically display a similar bimodal pattern, because of its finer resolution, we do not see this effect in the figures.

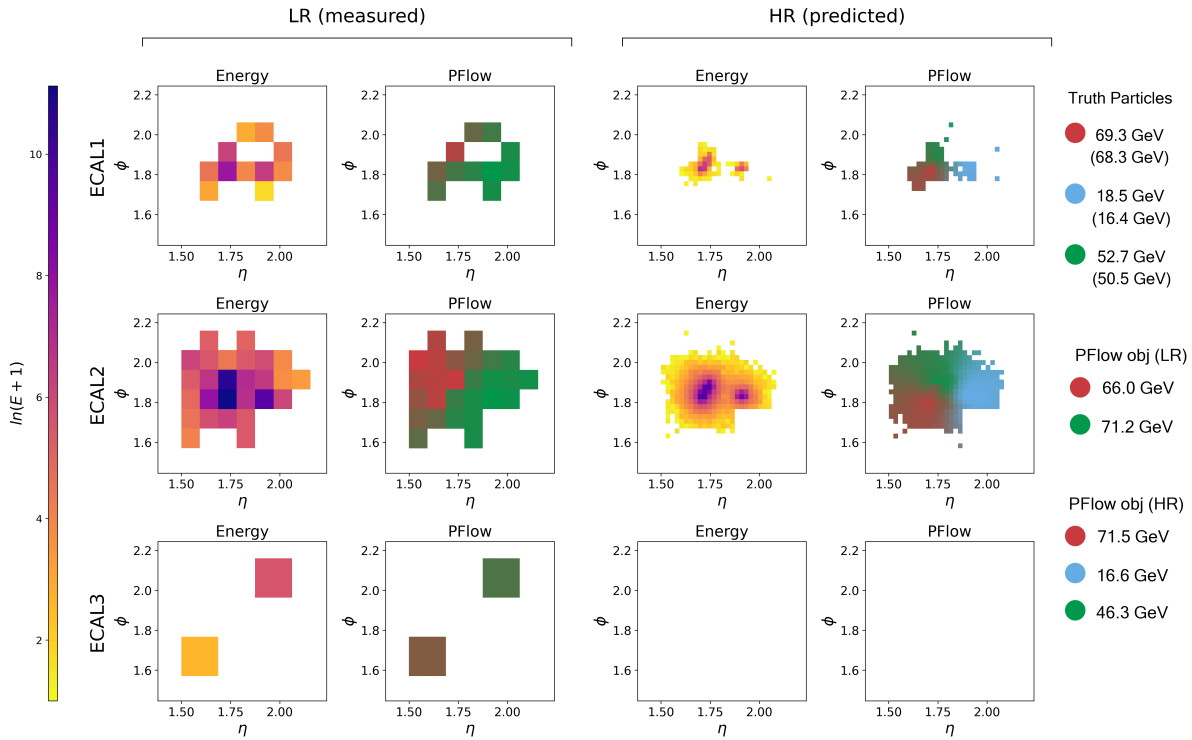


Figure 9: Event display illustrating the application of super-resolution on particle flow, as well as the interpretability of the particle reconstruction model. Each cell is assigned a fractional weight based on the predicted attention/incidence values, which determine the cell colors. The legend shows the truth and predicted particles with their energies. The true deposited energy for the truth particles are shown in parentheses. The particle flow model trained on the predicted high-resolution cells correctly identifies all three particles with very accurate energy estimations, while the model trained on low-resolution measured cells fails to disentangle the event into three particles and predicts only two particles.

Figure 9 presents a detailed event display showcasing the particle-flow model in action. In this case, the cardinality predictor is run first, and its output is fed into the kinematic predictor. Although the entire process occurs at the graph level, for clarity, we present the results in the $\eta - \phi$ plane as images.

5. Discussion

The results from the studies above indicate that super-resolution is a viable and promising approach for improving reconstruction. However, this raises the question of how these improvements should be understood.

Super-resolution or hallucination: A central question in this context is understanding where the network derives the “extra” information that enhances low-resolution inputs into high-resolution outputs. The key insight lies in the patterns learned from the training data, particularly the nature of electromagnetic (EM) showers. Although EM showers are stochastic on a case-by-case basis, they exhibit patterns that the network can learn to associate with high-resolution representations, essentially modeling the probability distribution $p(HR|LR)$.

However, a critical concern is ensuring that the network’s outputs are not just realistic-looking but also physically correct. While we can verify the accuracy of super-resolved outputs using Monte Carlo (MC) simulations, the challenge intensifies when working with real experimental data, where such direct comparisons are not feasible. In these cases, the focus shifts to calibration, aiming to align the SR model’s outputs with physical reality as closely as possible. Although this is challenging, we believe it is a solvable problem. For instance, in certain cases where constructing a full high-resolution detector isn’t feasible, it might still be possible to develop a small, high-resolution prototype module. This could be used to validate the network’s outputs, providing a benchmark for assessing the model’s performance.

Super-resolution as an auxiliary task: Moreover, super-resolution should be considered not just as an independent task but as an auxiliary to the broader reconstruction processes. By guiding the network to focus on relevant features, super-resolution can complement traditional reconstruction algorithms, which explains why LR PFlow performance lags behind HR PFlow. In this paper, we explored SR as a preprocessing task, but it could also be embedded as a component of the PFlow training objective. The integration of SR techniques in this way has the potential to inform future detector designs and enhance the development of reconstruction algorithms, ultimately leading to more accurate and reliable data interpretation in collider experiments.

Future directions: Going forward, we plan to investigate more realistic and complete physics setups, including hadronic showers. Incorporating hadronic showers will introduce greater complexity due to the increased fluctuations inherent in these processes. As we progress toward a full event analysis, the rise in cardinality will present additional challenges, where limited graph connectivity may prove advantageous. Furthermore, we aim to explore super-resolution in the lateral direction, where the number of calorimeter layers will also be upscaled.

6. Conclusion

In this work, we demonstrated, for the first time, that super-resolution techniques can be seamlessly integrated into the standard LHC-like reconstruction pipeline. We introduced a novel graph-based model for super-resolution that leverages the powerful flow matching framework alongside a transparent and interpretable particle flow model. However, the key takeaway is not the specific models employed; rather, it's that super-resolution can indeed enhance reconstruction. Our approach faithfully replicates high-resolution cell distributions, leading to significantly improved modeling of cell substructure variables. Moreover, utilizing these high-resolution cells for particle flow substantially enhances both particle cardinality and kinematics performance. We believe these findings could significantly impact the reconstruction pipelines of current LHC-like experiments and could be a major consideration in future detector design.

Acknowledgement

We would like to thank Dmitrii Kobilianskii for fruitful discussions on flow matching implementation, and Kyle Cranmer and Yihui Ren for their valuable insights. EG also acknowledges support from ISF Grant 2871/19, the BSF-NSF Grant 2020780 and the Weizmann Institute of Science and Mohamed bin Zayed University of Artificial Intelligence collaboration grant. We also thank the Benozio center for High Energy Physics for supporting our research.

Authorship statement

The author contribution according to Contributor Roles Taxonomy (CRediT) is as follows. **Nilotpal Kakati:** conceptualization, methodology, software, validation, formal analysis, investigation, data curation, writing - original draft, visualization. **Etienne Dreyer:** investigation, formal analysis, data curation, writing - review & editing. **Eilam Gross:** investigation, formal analysis, writing - review & editing, supervision, funding acquisition.

Code availability

The code for this paper can be found at <https://github.com/nilotpal09/SuperResolutionHEP>

References

- [1] Lyndon Evans and Philip Bryant. LHC Machine. *JINST*, 3:S08001, 2008.
- [2] ATLAS collaboration. Jet reconstruction and performance using particle flow with the ATLAS Detector. *Eur. Phys. J. C*, 77(7):466, 2017.
- [3] CMS collaboration. Particle-flow reconstruction and global event description with the CMS detector. *JINST*, 12(10):P10003, 2017.
- [4] Huong Lan Tran, Katja Krüger, Felix Sefkow, Steven Green, John Marshall, Mark Thomson, and Frank Simon. Software compensation in Particle Flow reconstruction. *Eur. Phys. J. C*, 77(10):698, 2017.
- [5] Chao Dong, Chen Change Loy, Kaiming He, and Xiaoou Tang. Image super-resolution using deep convolutional networks. *IEEE Transactions on Pattern Analysis and Machine Intelligence*, 38(2):295–307, 2016.
- [6] Jiwon Kim, Jung Kwon Lee, and Kyoung Mu Lee. Accurate image super-resolution using very deep convolutional networks. In *2016 IEEE Conference on Computer Vision and Pattern Recognition (CVPR)*, pages 1646–1654, 2016.
- [7] Bee Lim, Sanghyun Son, Heewon Kim, Seungjun Nah, and Kyoung Mu Lee. Enhanced deep residual networks for single image super-resolution. In *2017 IEEE Conference on Computer Vision and Pattern Recognition Workshops (CVPRW)*, pages 1132–1140, 2017.
- [8] Christian Ledig, Lucas Theis, Ferenc Huszár, Jose Caballero, Andrew Cunningham, Alejandro Acosta, Andrew Aitken, Alykhan Tejani, Johannes Totz, Zehan Wang, and Wenzhe Shi. Photo-realistic single image super-resolution using a generative adversarial network. In *2017 IEEE Conference on Computer Vision and Pattern Recognition (CVPR)*, pages 105–114, 2017.
- [9] Yulun Zhang, Kunpeng Li, Kai Li, Lichen Wang, Bineng Zhong, and Yun Fu. Image super-resolution using very deep residual channel attention networks. In Vittorio Ferrari, Martial Hebert, Cristian Sminchisescu, and Yair Weiss, editors, *Computer Vision – ECCV 2018*, pages 294–310, Cham, 2018. Springer International Publishing.
- [10] Xintao Wang, Ke Yu, Shixiang Wu, Jinjin Gu, Yihao Liu, Chao Dong, Yu Qiao, and Chen Change Loy. Esrgan: Enhanced super-resolution generative adversarial networks. In Laura Leal-Taixé and Stefan Roth, editors, *Computer Vision – ECCV 2018 Workshops*, pages 63–79, Cham, 2019. Springer International Publishing.
- [11] Chitwan Saharia, Jonathan Ho, William Chan, Tim Salimans, David J. Fleet, and Mohammad Norouzi. Image super-resolution via iterative refinement. *IEEE Transactions on Pattern Analysis and Machine Intelligence*, 45(4):4713–4726, 2023.
- [12] Francesco Armando Di Bello, Sanmay Ganguly, Eilam Gross, Marumi Kado, Michael Pitt, Lorenzo Santi, and Jonathan Shlomi. Towards a computer vision particle flow. *The European Physical Journal C*, 81(2):107, Feb 2021.

- [13] Pierre Baldi, Lukas Blecher, Anja Butter, Julian Collado, Jessica N. Howard, Fabian Keilbach, Tilman Plehn, Gregor Kasieczka, and Daniel Whiteson. How to GAN Higher Jet Resolution. *SciPost Phys.*, 13:064, 2022.
- [14] Ian Pang, David Shih, and John Andrew Raine. Calorimeter shower superresolution. *Phys. Rev. D*, 109:092009, May 2024.
- [15] Johannes Erdmann, Aaron van der Graaf, Florian Mausolf, and Olaf Nackenhorst. Sr-gan for sr-gamma: super resolution of photon calorimeter images at collider experiments. *The European Physical Journal C*, 83(11):1001, Nov 2023.
- [16] Felix J. Yu, Nicholas Kamp, and Carlos A. Argüelles. Enhancing events in neutrino telescopes through deep learning-driven super-resolution, 2024.
- [17] Yanting Yin, Yajing Wu, Xuebing Yang, Wensheng Zhang, and Xiaojie Yuan. Super resolution graph with conditional normalizing flows for temporal link prediction. *IEEE Transactions on Knowledge and Data Engineering*, 36(3):1311–1327, 2024.
- [18] Nishant Rajadhyaksha and Islem Rekik. Diffusion-Based Graph Super-Resolution with Application to Connectomics. In *Predictive Intelligence in Medicine*, pages 96–107, Cham, 2023. Springer Nature Switzerland.
- [19] F. A. Di Bello, E. Dreyer, S. Ganguly, E. Gross, L. Heinrich, et al. Reconstructing particles in jets using set transformer and hypergraph prediction networks. *Eur. Phys. J. C*, 83(7):596, 2023.
- [20] F. A. Di Bello, A. Charkin-Gorbulin, K. Cranmer, E. Dreyer, S. Ganguly, et al. Configurable calorimeter simulation for AI applications. *Machine Learning: Science and Technology*, 4(3):035042, 2023.
- [21] S. Agostinelli et al. GEANT4—a simulation toolkit. *Nucl. Instrum. Meth. A*, 506:250–303, 2003.
- [22] John Allison et al. Geant4 developments and applications. *IEEE Trans. Nucl. Sci.*, 53:270, 2006.
- [23] J. Allison et al. Recent developments in Geant4. *Nucl. Instrum. Meth. A*, 835:186–225, 2016.
- [24] E. Moyse, F. Ali, E. Cortina, R. M. Bianchi, and B. Couturier. The Phoenix event display framework. *EPJ Web Conf.*, 251:01007, 2021.
- [25] Ricky T. Q. Chen, Yulia Rubanova, Jesse Bettencourt, and David K Duvenaud. Neural ordinary differential equations. In S. Bengio, H. Wallach, H. Larochelle, K. Grauman, N. Cesa-Bianchi, and R. Garnett, editors, *Advances in Neural Information Processing Systems*, volume 31. Curran Associates, Inc., 2018.
- [26] Yaron Lipman, Ricky T. Q. Chen, Heli Ben-Hamu, Maximilian Nickel, and Matthew Le. Flow matching for generative modeling. In *The Eleventh International Conference on Learning Representations*, 2023.
- [27] Alexander Tong, Kilian FATRAS, Nikolay Malkin, Guillaume Huguet, Yanlei Zhang, Jarrod Rector-Brooks, Guy Wolf, and Yoshua Bengio. Improving and generalizing flow-

- based generative models with minibatch optimal transport. *Transactions on Machine Learning Research*, 2024. Expert Certification.
- [28] Ricky T. Q. Chen. torchdiffeq. <https://github.com/rtqichen/torchdiffeq>.
 - [29] William S. Peebles and Saining Xie. Scalable diffusion models with transformers. *2023 IEEE/CVF International Conference on Computer Vision (ICCV)*, pages 4172–4182, 2022.
 - [30] Claudius Krause and David Shih. Fast and accurate simulations of calorimeter showers with normalizing flows. *Phys. Rev. D*, 107:113003, Jun 2023.
 - [31] Ilya Loshchilov and Frank Hutter. Decoupled weight decay regularization. In *International Conference on Learning Representations*, 2017.
 - [32] J. Kieseler. Object condensation: one-stage grid-free multi-object reconstruction in physics detectors, graph, and image data. *Eur. Phys. J. C*, 80(9):1–12, 2020.
 - [33] S. R. Qasim, J. Kieseler, Y. Iiyama, and M. Pierini. Learning representations of irregular particle-detector geometry with distance-weighted graph networks. *Eur. Phys. J. C*, 79(7):608, 2019.
 - [34] S. R. Qasim, K. Long, J. Kieseler, M. Pierini, and R. Nawaz. Multi-particle reconstruction in the High Granularity Calorimeter using object condensation and graph neural networks. *EPJ Web Conf.*, 251:03072, 2021.
 - [35] S. R. Qasim, N. Chernyavskaya, J. Kieseler, K. Long, O. Viazlo, M. Pierini, and R. Nawaz. End-to-end multi-particle reconstruction in high occupancy imaging calorimeters with graph neural networks. *Eur. Phys. J. C*, 82(8):753, 2022.
 - [36] J. Pata, J. Duarte, J. R. Vlimant, M. Pierini, and M. Spiropulu. MLPF: Efficient machine-learned particle-flow reconstruction using graph neural networks. *Eur. Phys. J. C*, 81(5):1–14, 2021.
 - [37] J. Pata, J. Duarte, F. Mokhtar, E. Wulff, J. Yoo, J. R. Vlimant, M. Pierini, and M. Girone. Machine Learning for Particle Flow Reconstruction at CMS. *J. Phys. Conf. Ser.*, 2438(1):012100, 2022.
 - [38] F. Mokhtar, J. Pata, J. Duarte, E. Wulff, M. Pierini, and J. R. Vlimant. Progress towards an improved particle flow algorithm at CMS with machine learning. In *ACAT 2022*, 3 2023.
 - [39] J. Pata, E. Wulff, F. Mokhtar, D. Southwick, M. Zhang, M. Girone, and J. Duarte. Improved particle-flow event reconstruction with scalable neural networks for current and future particle detectors. 9 2023.
 - [40] H. W. Kuhn. The Hungarian method for the assignment problem. *Naval research logistics quarterly*, 2(1-2):83–97, 1955.
 - [41] Andrew J. Larkoski, Gavin P. Salam, and Jesse Thaler. Energy Correlation Functions for Jet Substructure. *JHEP*, 06:108, 2013.
 - [42] Andrew J. Larkoski, Ian Moulton, and Duff Neill. Power Counting to Better Jet Observables. *JHEP*, 12:009, 2014.